Article | Received 29 June 2025; Revised 17 August 2025; Accepted 30 August 2025; Published 12 September 2025
https://doi.org/10.55092/sc20250024

Multi-interface effects on mechanical behavior in 3D-printed concrete shear keys: a finite element modeling strategy

Xin Tian[1,†], Anqi Shi[2,†], Zhi Fang[1,3,*] and Alexander Lin[2,*]

[1] College of Civil Engineering, Hunan University, Changsha 410082, China
[2] Department of the Built Environment, College of Design and Engineering, National University of Singapore, Singapore 117566, Singapore
[3] Key Laboratory for Wind and Bridge Engineering of Hunan Province, Changsha 410082, China

† These authors contributed equally to this work.

* Corresponding authors; E-mails: fangzhi@hnu.edu.cn (Z.F.), bdgal@nus.edu.sg (A.L.).

Highlights:

- A finite element model suitable for 3D-printed concrete components that accounts for multi-interface conditions is established.
- Four 3D-printed concrete shear keys with different key angles are used to validate the proposed models.
- 3DPC shear keys with lower key angles show higher shear strength.

Abstract: With the rapid advancement of 3D printing technology, one of its widely adopted practical applications is the assembly of buildings using 3D-printed modular components. This method involves printing structural element formworks and subsequently casting concrete and arranging steel reinforcement within them to achieve reinforced 3D-printed concrete (3DPC) components. Therefore, research on connectors between modular structural components, *i.e.*, 3DPC shear keys, is particularly important. Given the limitations and complexities of experimental studies on 3D printing, establishing a three-dimensional finite element model capable of accurately capturing the mechanical behavior of 3D-printed components is also crucial. This paper provides a brief overview of the research group's previous large-scale experimental studies on 3DPC shear keys. The commercial finite element software ABAQUS is used for modeling and analyzing of test specimens, leading to the establishment of a finite element model suitable for 3DPC components that accounts for multi-interface conditions. By considering different interface behaviors, the analysis results indicate that the model incorporating both interface cohesion and friction behavior yields the most accurate predictions with an average predicted-to-experimental ratio of 0.99 and 0.86 for peak load and deflection, respectively. Besides, lower key angles show higher shear strength due to the longer contact path and higher normal force at the interface, which leads to higher friction and interfacial force with an enhancement in shear strength of 10.4%. These findings establish a reliable modeling framework for precise evaluation of 3DPC joint performance, thereby providing actionable guidance for optimizing modular connections in prefabricated construction.

Keywords: 3D-printed concrete; shear key; finite element method; multi-interface; mechanical behavior

1. Introduction

In recent years, 3D printed concrete (3DPC) has emerged as a novel construction approach that differs fundamentally from conventional formwork-based casting methods. By enabling the direct fabrication of complex geometries without the need for formwork, 3DPC not only reduces material consumption and shortens construction time, but also significantly improves the flexibility of structural customization and enhances overall construction efficiency [1,2].

However, due to the limitations in the size and operational range of current 3D printing equipment, the printable dimensions are often smaller than the overall scale required for real-world construction applications. As a result, multiple printed components must typically be assembled to form a complete structural system. This prefabricated assembly approach imposes more stringent demands on the design of connection mechanisms, where interlocking strategies play a critical role in ensuring effective load transfer and structural cooperation between adjacent elements. Among these, shear keys represent one of the most widely adopted interlocking features. By utilizing geometric interlocking at the interface, shear keys effectively resist shear forces, prevent relative displacement or misalignment between components, and thereby enhance the structural integrity and reliability of load transmission [3,4].

In practical construction, shear keys are often composed of segments made from different materials or fabricated through varying processes, resulting in multi-material and multi-interface characteristics [5]. These features lead to complex load-bearing behavior and significant localized stress concentrations, making shear keys potential weak points in structural systems. Therefore, a systematic evaluation of their mechanical performance is necessary. Existing studies have examined the behavior of 3DPC shear keys from multiple perspectives, including interfacial strength, ultimate load-bearing capacity, and failure modes. To evaluate the tensile strength of the interlocking interface, Wang *et al.* have employed axial compression-splitting tests combined with Digital Image Correlation (DIC) and compression-shear tests conducted under both displacement-controlled and force-controlled conditions [6].

Several studies have focused on the mechanical enhancement of interlayer interfaces/joints for 3DPC. One investigation developed a tailored printing process and specialized nozzle to achieve interlayer interlocking, with extrudability tests conducted to determine optimal printing parameters. Subsequent compressive, interfacial splitting, and interlayer interfacial shear tests demonstrated that interlocking interfaces increased splitting tensile strength by approximately 14.5%–30.7%, shear strength by 7.8%–18.0%, and reduced the anisotropy coefficient by about 13.7%–25.5%, thereby significantly mitigating anisotropy; notably, the nozzle with a 135° tooth angle achieved superior compactness and interface strength [7]. Another study optimized interlayer joints through sinusoidal, square, and inclined interlocking textures, with tensile and compressive tests along three orthogonal directions confirming the sinusoidal form as most effective for enhancing strength and reducing anisotropy [8]. A further investigation employed a modified L-type shear test method to systematically evaluate the effects of recycled sand replacement ratio, printing interval, and surface treatment on the bond performance of both interlayer and interstrip interfaces, finding comparable strengths under identical conditions, but significant degradation with recycled sand use and prolonged printing intervals, while epoxy grout proved most effective in strengthening [9]. Additionally, a study involving specimens with varying layer inclinations and ages, each incorporating a 30-minute cold joint, employed modified slant shear tests to define the Mohr's envelope for layered 3DPC, identifying layer inclinations of 60° and 75° as an interface-failure-dominated range, with a friction angle (approximately 46°) comparable

to values reported for 3DPC matrices in other studies and a cohesion approximately 10% lower, resulting in slight anisotropy in strength [10].

Following the aforementioned 3DPC joint tests, one of the corresponding author's team employed a hybrid manufacturing process combining 3DPC and casting to produce shear keys with complex shear key shapes and different key angles [4] and quantified the ultimate load-bearing capacity and the distribution of surface cracks. However, the stress field and crack distribution alongside the intricately shaped key region and the complex interaction behavior between the multi-interfaces were not well captured due to the limitations of experimental measurements.

Experimental techniques exhibit significant limitations in revealing the internal mechanical behavior of structural components. While DIC can provide full-field deformation information, its application is confined to the two-dimensional surface layer, making it difficult to capture the stress-strain evolution within the internal structure. Strain gauges and displacement sensors, although useful, yield discrete data points that fail to represent the continuous distribution of the mechanical field in complex regions. Load sensors, on the other hand, can record the overall force response but cannot present the local stress paths or the origin of crack initiation. Consequently, relying solely on experimental data is insufficient for a comprehensive understanding of the three-dimensional stress state, crack development paths, and the intricate interaction between multiple interfaces in shear key regions.

To address the limitations in data dimensionality and spatial resolution inherent in experimental methods, this study introduces Finite Element Analysis (FEA) to conduct detailed modeling and simulation of the micro-stress field distribution, crack evolution paths, and multi-interface coupling behaviors within the shear key region. Through numerical simulation, the study not only supplements the internal structural responses that cannot be observed during experiments but also provides a deeper, systematic understanding of the mechanical behavior of 3DPC prefabricated connection components. This, in turn, enhances the precision and reliability of design processes.

Numerous numerical studies have been conducted to model structural members involving interface interactions, such as composite components [11], strengthened pre-damaged components [12,13], and push-off tests on concrete-cast shear keys [14]. Zhang [14] and Shamass [15] performed numerical analyses of push-off tests on concrete-cast shear keys using the CDP model in ABAQUS with surface interaction only including friction. The average value for the numerical-to-experimental ultimate strength ratio is 0.91 [15], indicating an underestimation of the shear key strength due to the absence of cohesion in their models. Similarly, Rousan *et al.* [16] adopted the same modeling strategy but overestimated the ultimate strength and exhibited a higher softening segment. Further research simulated surface contact containing both cohesion and friction. Zhan [17] investigated direct shear tests on keyed tooth and concrete-cast joints with epoxy layers, achieving remarkable accuracy in prediction. However, they did not mention the definition process of their interface parameters. Neirinck [18] employed similar modeling strategies and all their interaction parameters came from the direct tension tests, slant shear tests, and bi-shear tests. Their model, however, focused on the long-term performance of box girder bridges under temperature gradients and not for mechanical behavior.

Recently, Hussein [19] determined the interface cohesion and friction parameters by numerical simulations of direct tension and slant shear tests. Then, these parameters were validated via comparison with laboratory tests on adjacent box-beams. Further comparative studies on push-off tests of concrete-cast shear keys confirmed their FEM models [20,21]. Zhu [12,13] conducted numerical research on strengthening

pre-damaged components. They found that the proposed interface model by Hussein [19] has precise accuracy in modeling their specimens.

In summary, the above-mentioned finite element modeling of shear keys incorporating both friction and cohesion has shown superior predictive accuracy for conventional concrete-cast shear keys. To the authors' knowledge, no research has yet established a finite element model for 3DPC shear keys, which involve more complex surface contact conditions due to surface contact between 3D-printed filaments and cast concrete core. To address the question of how best to model the behavior of this type of component, this study proposes a modelling strategy for 3DPC shear keys that considers different surface interactions, *i.e.*, surface between printed concrete, casted concrete, and key regions, which other research did not consider. Besides, the interface parameters are derived from 3D-printed slant shear tests previously conducted by the authors [4]. Then, the established FEM models are validated by the large-scale 3DPC shear keys per previous study [4] to show the applicability of the proposed model and calculated interface parameters in the prediction of 3DPC shear keys.

2. A previous experimental study as a basis for the present simulation

This section describes a previous study that conducted push-off experiments on 3DPC shear keys [4], which serves as the basis for, and will be compared with, the finite element simulations in the present study. In these push-off experiments, all specimens were fabricated using identical mortar material. The cementitious matrix consisted of Type 1 Portland cement, silica sand (fineness modulus = 0.1), water, and ADVA-181 polycarboxylate-based superplasticizer, with a mass ratio of 1:0.6:0.4:0.002, respectively. After a standard 28-day moist curing, the hardened mortar exhibited a compressive strength of 44.2 MPa and a splitting tensile strength of 3.05 MPa. In addition, Mapefix EP 385 was utilized as a bonding agent, offering a compressive strength of 120 MPa, a flexural strength of 42 MPa, and an elastic modulus of 10,800 MPa [4].

The study specifically focuses on the influence of shear key geometry on mechanical performance, comparing push-off tests of trapezoidal shear keys with two distinct angles, 70.35° and 54.46°. Accordingly, the specimens are named M-DS-k70 and M-DS-k54, where "k70" and "k54" denote shear key angles of 70.35° and 54.46°, respectively. The abbreviation "DS" refers to such specimens subjected to direct shear loading, distinguishing them from another set of specimens tested under slant shear, which are labeled "SS." The SS specimens are part of a supplementary test program that will be introduced later.

Each configuration—*i.e.*, shear key specimens with angles of either 70.35° or 54.46°—consists of two interlocking components: one male and one female, as illustrated in Figure 1. The specimens had standardized dimensions: 340 mm in width, 635 mm in length, and 70 mm in thickness. The shear key bases measured 100 × 70 mm^2, with a consistent key depth of 35 mm. The 3DPC shear key geometry was designed to replicate the standard precast concrete shear key, enabling direct comparison between 3DPC and precast components. The chosen angles fall within the ranges reported in [22–24], while the base length and depth are identical to those in [22] and [23]. The specimens were produced using a hybrid manufacturing technique, combining 3DPC for the external shell and cast-in-place concrete for the core region. The 3DPC method was employed to construct the external shell, allowing for the precise formation of the trapezoidal shear key geometry. Consequently, various types of interfacial contacts were formed, such as the interface between 3D-printed concrete layers, between 3D-printed and cast-in-place concrete, and between epoxy and 3D-printed concrete, as illustrated in Figure 2. During the 3D printing process,

galvanized steel mesh with a grid size of 50 × 50 mm and a wire diameter of 4 mm was embedded into each printed layer. The core region was subsequently cast using in-situ concrete, and the casting process effectively bonded the steel mesh, the 3D-printed shell, and the core part into an integrated structure. This integration enhanced the overall structural performance, improved structural integrity, and prevented failure in regions not subjected to direct testing. In addition, the male and female shear key components were jointed using the previously mentioned Mapefix EP 385 adhesive to ensure sufficient interfacial strength and structural integration.

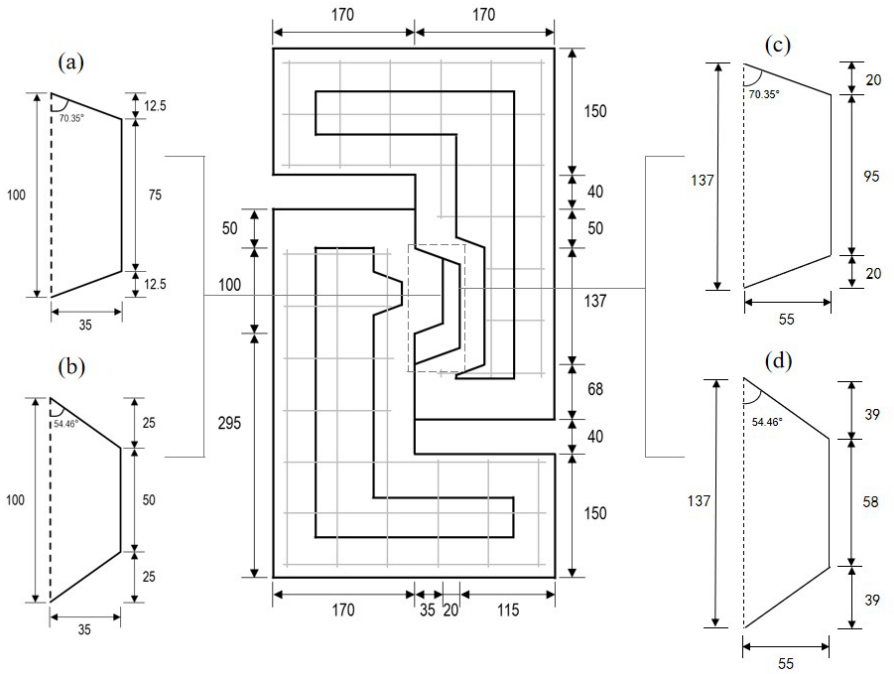

Figure 1. Dimensions of the specimens [4]: **(a)** male key of M-DS-k70, **(b)** male key of M-DS-k54, **(c)** female key of M-DS-k70, and **(d)** female key of M-DS-k54 (unit: mm).

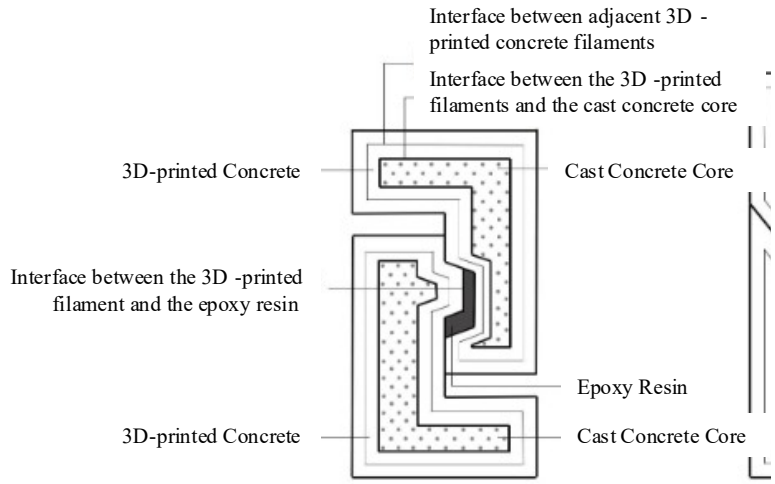

Figure 2. Schematic diagrams for push-off test specimens [4].

The experimental setup utilized a 500-KN capacity Instron Actuator (Figure 3). The specimens were primarily subjected to a load employing a machine head displacement rate of 0.40 mm/min. A constant horizontal confining pressure of 2 MPa—representative of the pressures typically experienced by prestressed concrete shear keys [25–28]—was maintained using dual-side hydraulic jack, and a steel roller conveyor positioned on the sides of the setup was used to eliminate vertical friction caused by the clamping fixtures. The specimens were coated with a hard plaster to create flat and smooth surfaces, ensuring that the stress distribution across these surfaces were uniform. Moreover, the relative displacement of the specimens was monitored using four displacement sensors arranged diagonally at the front and back of each specimen.

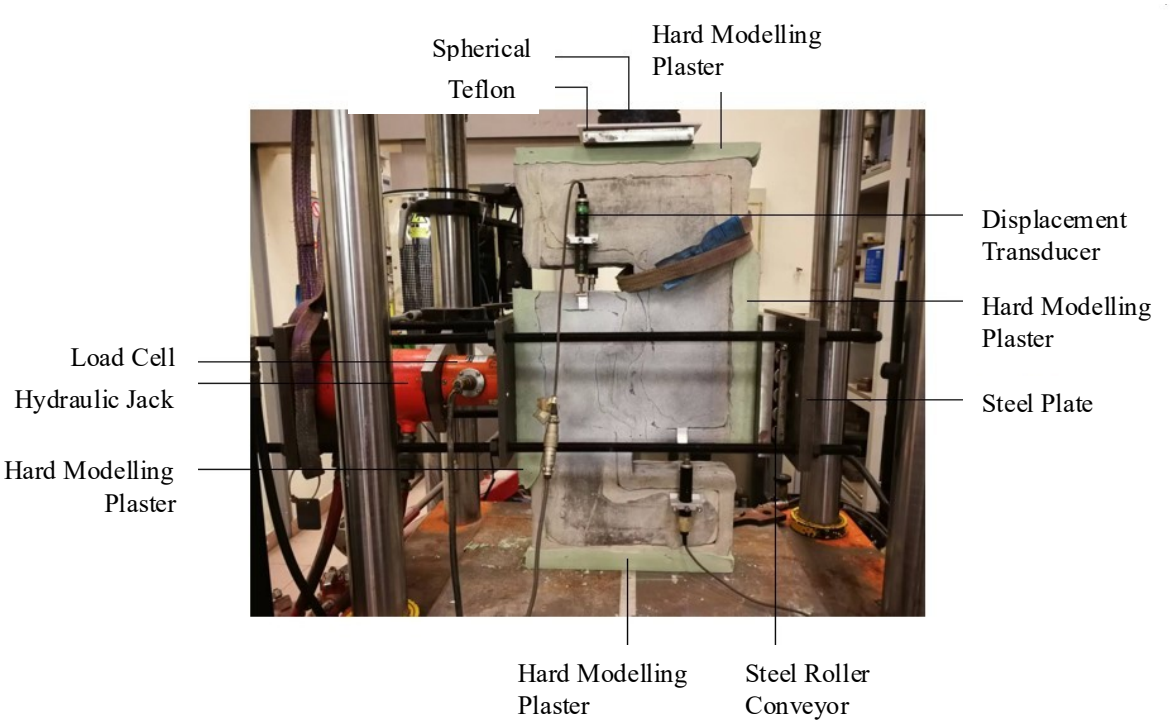

Figure 3. Diagram for test set-up [4].

2.1. Test results

Figure 4 shows the crack patterns for specimens with different shear key angles. The cracking processes occurred in the 3D-printed shear key specimens were same as that in the tests of precast shear keys respectively conducted by Zhou *et al.* [29] and Jiang *et al.* [7] whereby cracks initiated from both the top and bottom of the shear key before widening and propagating further resulting in the shear-off failure.

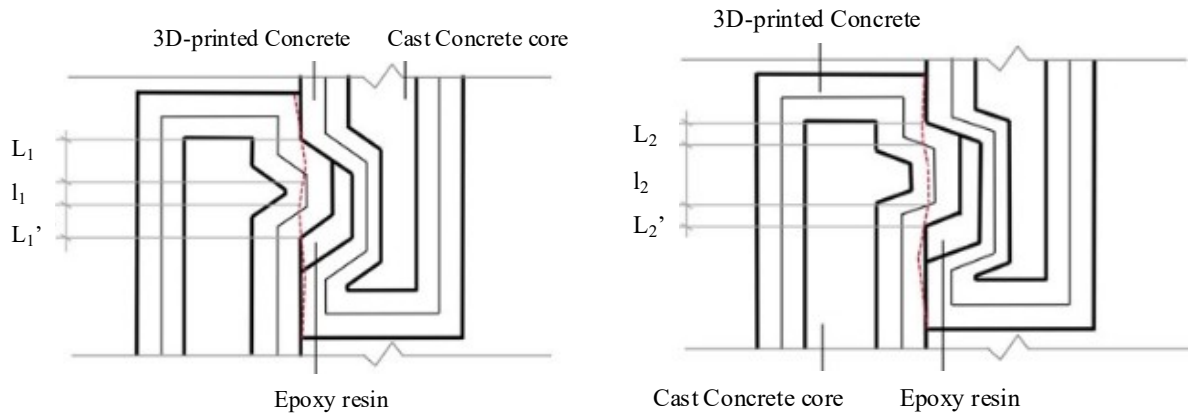

(a) (b)

Figure 4. Typical failure modes for 3DPC shear keys [4]: **(a)** M-DS-k54; and **(b)** M-DS-k70.

Figure 5 plots the load-deflection curves for M-DS-k54 and M-DS-k70. Since there are two parallel specimens at each angle, the last number in the abbreviation in the figure is the specimen number. All specimens had similar non-linear ascending curves followed by slightly different peak stresses and descending curves as the post peak failure process of the unreinforced shear keys was relatively brittle. The shear capacities of the specimens with different shear key angles are generally similar, but the specimen with a 54° shear key exhibits a slightly higher capacity. The shear capacity of the key depends on the relative lengths of the crack path that penetrate through the bulk 3D-printed concrete *versus* the interface between adjacent printed layers. This is because the interface behaves more like a cold joint and is generally weaker than the bulk material. The smaller shear key angle of 54.46° forces the shear crack to propagate through a longer path within the bulk 3D-printed concrete—denoted as L_1 and L_1' in Figure 4—and a shorter interface between adjacent 3D-printed layers, labeled l_1 in the figure. In contrast, a larger shear key angle of 70.35° causes the shear crack to traverse a longer segment along the weaker interfacial region—labeled l_2—while penetrating a shorter length through the bulk concrete, denoted as L_2 and L_2'. This shift in cracking path may reduce the overall resistance, as the interfacial region typically has lower strength compared to the bulk material.

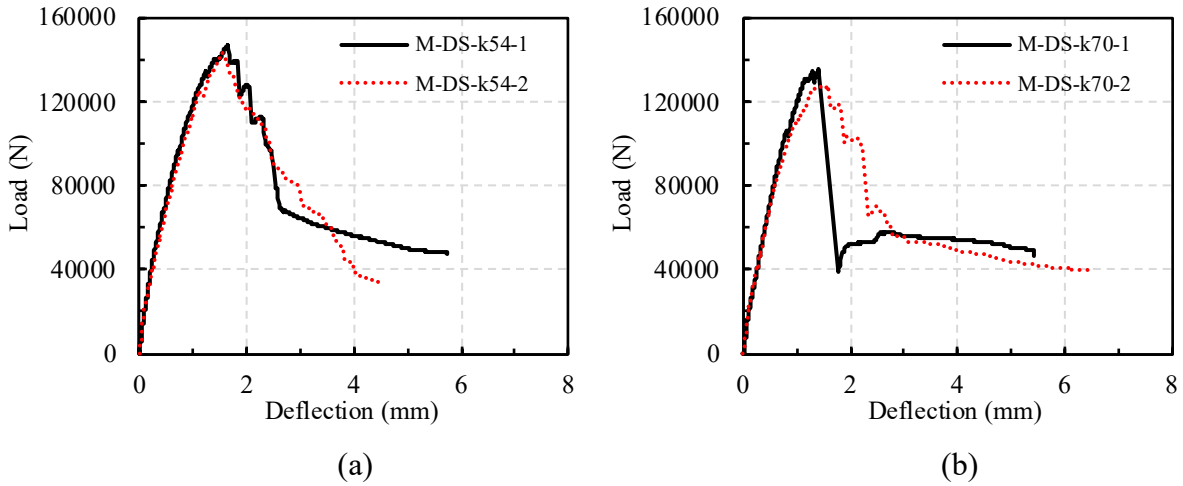

Figure 5. Load-deflection curves for 3DPC shear keys [4]: **(a)** M-DS-k54; and **(b)** M-DS-k70.

3. Modeling methodology

3.1. Shear key modeling

This section presents a numerical model for simulating 3DPC shear keys, building upon the authors' previous research [4]. Three-dimensional finite element models were developed in ABAQUS, which effectively captures the nonlinear compressive and tensile behavior of concrete structures [13,30]. Figure 6 illustrates the mesh discretization and geometry of the finite element model for a typical shear key filled with epoxy resin.

Concrete, steel load pads, and epoxy resin were modeled using three-dimensional eight-node elements (C3D8R) with a 10 × 10 × 10 mm element size (The mesh sensitivity analysis and element size determination are detailed in Section 5 below). Concrete was given the Concrete Damaged Plasticity (CDP) model, a well-established method, was used to simulate the nonlinear behavior of concrete under both compression and tension in ABAQUS [13]. Steel load pads were given a rigid material property with only elastic behavior. The epoxy resin was modeled as an elastic material with a modulus of 10,800 MPa [4].

The steel cages were modeled using 2-node linear 3-D truss elements (T3D2). These elements represent slender structural members that transmit only axial loads [31], exhibiting characteristics similar to those of the components within steel cages. The steel elements were embedded within the concrete elements, simulating perfect bonding between the steel reinforcements and concrete. The steel meshes were used to strengthen the 3DPC shear key and ensure failure at the interfaces between male and female keys.

The CDP model accurately captures the strain transition from an elastic state to an elastoplastic state and eventually reaches a fully plastic state. The plastic behavior of concrete in the CDP model is described through three key aspects: (1) the tensile behavior of normal-strength concrete (NC) after cracking is characterized by tensile stresses as a function of inelastic tensile strains; (2) the compressive behavior of NC is represented using yielding stresses and inelastic strains; (3) the corresponding tension and compression damage parameters, along with the failure surface which is defined by five plastic parameters, *i.e.*, flow potential eccentricity (M), the ratio of the second stress invariant on the tensile meridian to that on the compressive meridian (K_C), the ratio of the initial equiaxial compressive yield

stress to the initial uniaxial compressive yield stress (f_{bo}/f_{co}), viscosity (μ), and dilation angle (ϕ) [32–34]. Further details of the material constitutive models are provided in Section 4.

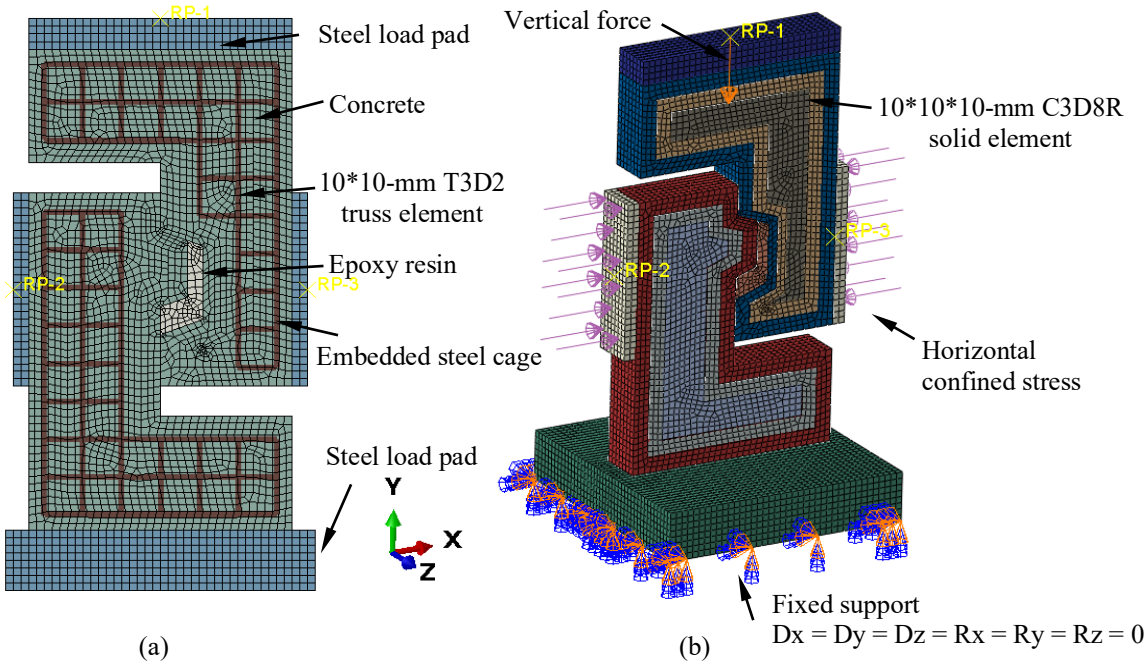

Figure 6. Finite-element model for a typical shear key: **(a)** front view; and **(b)** 3D model.

3.2. Loading and supporting boundaries modeling

A horizontal confinement stress of 2 MPa per [4] was applied using the surface pressure function during Step 1, referred to as 'preloading of confinement.' Loading conditions (one vertical loading plate and two horizontal loading plates) and support boundaries (one bottom support steel plate) were modeled to simulate the push-off tests under direct vertical loading, and each plate was modeled using elastic steel properties with C3D8R elements. The movement and rotation of the bottom steel plate were constrained to satisfy fixed boundary conditions.

3.3. Interface interaction modeling

Figure 7 illustrates the finite element model with different interface interactions, where different colors represent different 'Parts' in ABAQUS. The shear key comprises three components: the 3D-printed outer layer with two filaments, the casted concrete core, and the inner-filled epoxy resin. Accordingly, three types of surface contact were considered: (i) *Type 1 Interface* between two 3DPC filaments, (ii) *Type 2 interface* between inner 3DPC filament and casted concrete core, (iii) *Type 3 interface* between outer 3DPC filament and epoxy resin. Notably, the epoxy resin was used to fill the core gap and bond the outer 3DPC filaments for the male and female keys. Consequently, two distinct surface-to-surface contact interfaces involving epoxy bonding were defined: (1) the interface between the outer 3DPC filaments and the filled epoxy resin, and (2) the interface between the outer 3DPC filaments for the male and female keys.

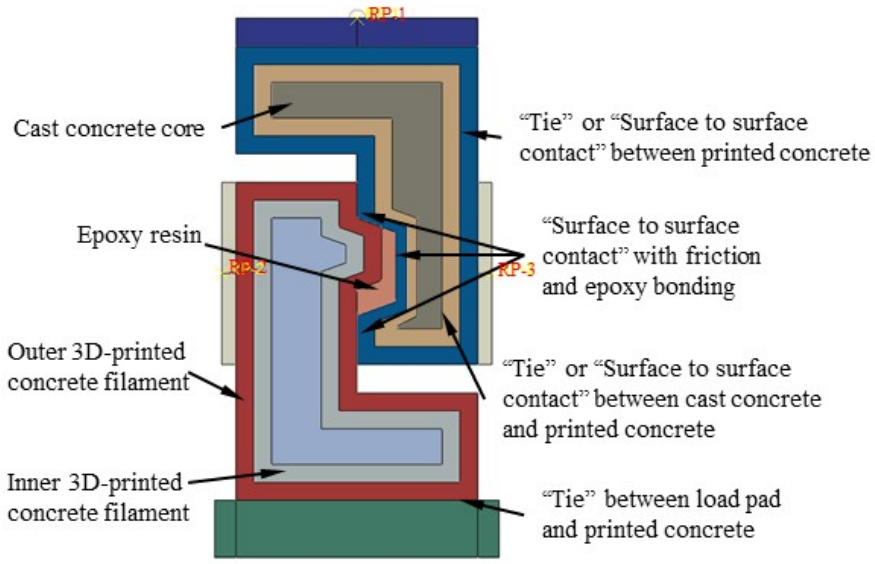

Figure 7. Interface interaction in the finite element model.

Two methods are used in existing design codes to define the shear stress at the interface between concrete elements. The first method, specified by AASHTO (American Association of State Highway and Transportation Officials) [35], considers three components of interface interaction: surface cohesion, surface friction, and shear reinforcement placed across the interface. The cohesion shear force c and friction coefficient μ are determined through laboratory tests such as slant shear tests or obtained from recommended values in AASHTO. The second method, outlined in ACI 318–19 [36], neglects cohesive strength. Therefore, only two parameters (*i.e.*, the friction coefficient and the shear reinforcement) are included in the calculation of shear strength.

ABAQUS provides a traction-separation model, shown in Figure 8, to simulate interface interactions through the "interaction contact" function. This approach models the interface as zero thickness, using surface-to-surface contact with defined surface properties to characterize various interface behaviors [13,19,37]. The surface properties used in the present study are listed in Table 1 and consist of three parts:

(1) Normal behavior: hard contact was defined, implying that no contact pressure is transmitted unless the nodes of the slave surface contact the master surface, no penetration is allowed at each constraint location, and no limit to the magnitude of contact pressure that can be transmitted when the surfaces are in contact.

(2) Tangential behavior: a friction coefficient (*i.e.*, a dimensionless scalar value that quantifies the resistance to relative sliding motion between two contacting surfaces) of 0.344, derived from slant shear tests conducted by the authors [4], was used for the concrete-epoxy interface. A recommended friction coefficient of 1.0 was used for interfaces with clean rough surfaces between 3DPC filaments and cast concrete core based on AASHTO [35].

(3) Cohesion: cohesion was defined using the traction-separation model, including stiffness K_n, K_s, and K_t, *i.e.*, normal stiffness, first tangential shear stiffness, and second tangential shear stiffness and "damage" (contact stresses, *i.e.*, the cohesion shear force, including t_n, t_s, and t_t, plastic displacement, and contact stabilization) in Abaqus [37]. The stiffnesses were set to match the elastic modulus of concrete, *i.e.*, 31,247 MPa per material tests on reference [4], ensuring sufficient stiffness to avoid

surface penetration. The contact stresses were set to the cohesion strength (c) of 5.92 MPa, calculated through slant shear tests. The total plastic displacement (*i.e.*, the residual displacement after peak load) was set as the measured value in reference [4]. Contact stabilization (*i.e.*, a parameter that prevents unrealistic oscillations or divergence when simulating contact interactions between surfaces) was set as the recommended value in reference [13], *i.e.*, 0.001. Additionally, only small sliding was permitted to avoid convergence issues arising from interface distortion.

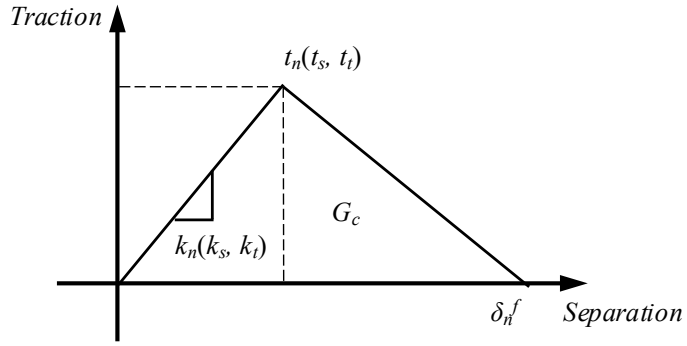

Figure 8. Traction-separation model of concrete interface.

Table 1. Mechanical properties of NSC interface with epoxy based on slant shear tests.

Parameters	Value
K_n, K_s, and K_t, N/mm^3	31247
t_n, t_s, and t_t, MPa	5.92
Total/plastic displacement δ_n^f, mm	0.6/0.2
Contact stabilization	0.001
Friction coefficient	0.344

The Mohr-Coulomb failure criterion was used to determine the cohesion shear force c and friction coefficient μ. Then, the corresponding parameters can be calculated based on the slant shear (SS) test results listed in Table 2. Other researchers have similarly employed slant shear tests to establish Mohr-Coulomb failure criteria for interface characterization. For instance, Hussein [17] determined the interface parameters by numerical simulations of direct tension and slant shear tests. Then, these parameters were validated via comparison with tests on adjacent box-beams. Zhu [10,11] used the proposed interface model by Hussein [17] to simulate pre-damaged components. They found that it gave proper accuracy.

$$\tau_u = \mu\sigma_n + c \quad (1) \tag{1}$$

where τ_u = peak shear stress at interface, MPa; σ_n = normal stress at interface, MPa.

Table 2. Slant shear test results for specimens with shear failures [4].

Specimen	Ultimate shear load, kN	Peak shear stress τ_u, MPa	Normal stress σ_n, MPa
M-SS-i55-1	214.24	7.80	5.47
M-SS-i60-2	219.89	7.39	4.26

Note: "SS" = slant shear test; "i" = inclination angle; "1" and "2" = the first and second specimens.

In addition to interaction contact, the 'Tie' in ABAQUS was employed to simulate the interface with simpler settings. This approach binds two interfaces together, preventing relative sliding. In this way, the authors aimed to investigate whether the complex contact behavior influences the prediction of shear key. Notably, 'Tie' was only used at the interface between the 3DPC filaments and the cast concrete core, as prohibiting sliding in the shear key connection region would not be realistic.

3.4. Loading application

A nonlinear static analysis with incremental displacement-based loading was conducted, considering geometric nonlinearity. The top rigid plate's surface at the loading points was coupled to a reference point for applying displacement. The step size for each incremental displacement was set to 0.006 mm to ensure computational convergence, considering the numerous contact interactions in the model. When the total load step reaches 1.0, the applied displacement reaches the target displacement, which means the calculation process is completed.

4. Material constitutive models

4.1. Concrete damage plasticity model of normal-strength concrete (NSC)

The widely adopted CDP model in ABAQUS was used to simulate the nonlinear behavior of NSC under compression and tension. The stress-strain curves and damage evolution equations for NSC under uniaxial tension and compression were derived based on the Chinese design code for concrete structures (GB/T50010-2010) [38].

Equations (2)–(5) present the derivation procedures for the tensile stress-strain relationships and damage evolution equations of NSC,

$$\sigma_t = (1-d_t)E_c\varepsilon_t \tag{2}$$

$$d_t = \begin{cases} 1-\rho_t\left[1.2-0.2x^5\right] & x \le 1 \\ 1-\dfrac{\rho_t}{\alpha_t(x-1)^{1.7}+x} & x > 1 \end{cases} \tag{3}$$

$$x = \frac{\varepsilon_t}{\varepsilon_{t,r}} \tag{4}$$

$$\rho_t = \frac{f_{t,r}}{E_t\varepsilon_{t,r}} \tag{5}$$

where σ_t = tensile stress, MPa; ε_t = tensile strain, mm / mm; E_c = elastic modulus, MPa; d_t = tensile damage parameter; $f_{t,r}$ = peak tensile strength of NSC, which is measured by material tests or calculated based on compressive strength $f_{t,r} = 0.394\sqrt{f_{c,r}}$, 3.05 MPa in present study; $\varepsilon_{t,r}$ = tensile strain at peak point, $\varepsilon_{t,r} = f_{t,r}^{\ 0.54} \times 65 \times 10^{-6}$; α_t = tensile parameters, $\alpha_t = 0.312 f_{t,r}^{\ 2}$.

Equations (6)–(10) present the derivation procedures for the compressive stress-strain relationships and damage evolution equations of NSC,

$$\sigma_c = (1-d_c)E_c\varepsilon_c \tag{6}$$

$$d_c = \begin{cases} 1-\dfrac{\rho_c n}{n-1+x^n} & x \le 1 \\ 1-\dfrac{\rho_c}{\alpha_c(x-1)^2+x} & x > 1 \end{cases} \tag{7}$$

$$x = \frac{\varepsilon_c}{\varepsilon_{c,r}} \tag{8}$$

$$\rho_c = \frac{f_{c,r}}{E_c\varepsilon_{c,r}} \tag{9}$$

$$n = \frac{E_c\varepsilon_{c,r}}{E_c\varepsilon_{c,r} - f_{c,r}} \tag{10}$$

where σ_c = compressive stress, MPa; ε_c = compressive strain, mm / mm; E_c = elastic modulus, MPa; d_c = compressive damage parameter; $f_{c,r}$ = peak compressive strength of NSC, which is measured from material tests, 44.23 MPa in present study; $\varepsilon_{c,r}$ = compressive strain at peak point, $\varepsilon_{c,r} = (172 f_{c,r}^{\ 0.5} + 700)\times 10^{-6}$; α_c = compressive parameters, $\alpha_c = 0.157 f_{t,r}^{\ 0.785} - 0.905$.

The elastic modulus of normal-strength concrete was estimated by ACI 318–19 [36]:

$$E_c = 4700\sqrt{f_c'} \tag{11}$$

The calculated stress-strain relationships for NSC under tension and compression are presented in Figure 9. According to the ABAQUS user manual, the stress-strain relationships of NSC must be converted to stress-inelastic strain relations to be compatible with CDP model in ABAQUS. The corresponding inelastic strain was calculated by the following Equations (12) and (13). The stress-inelastic strain values of NSC and UHPC are summarized in Table 3.

$$\varepsilon_c^{in} = \varepsilon_c - \frac{\sigma_c}{E_c} \tag{12}$$

$$\varepsilon_t^{in} = \varepsilon_t - \frac{\sigma_t}{E_c} \tag{13}$$

where ε_c^{in} and ε_t^{in} = inelastic compressive strain and cracking tensile strain, respectively, mm / mm.

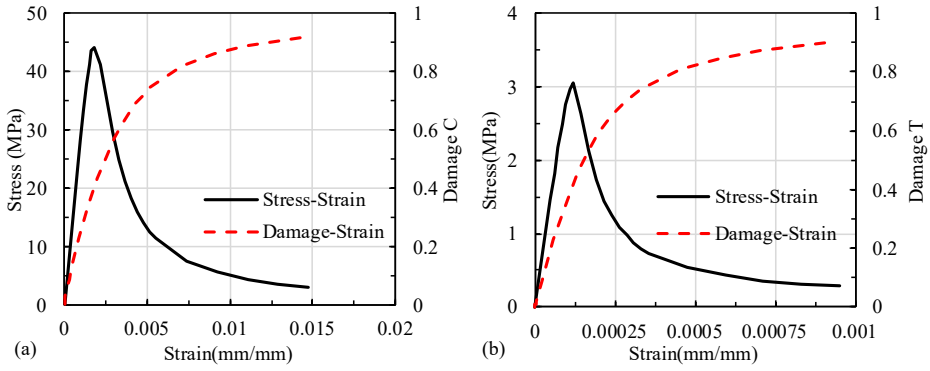

Figure 9. Stress-strain and damage evolution model for NSC: **(a)** compression; and **(b)** tension.

Table 3. CDP models for NSC in compression and tension.

Compression behavior of NSC			Tension behavior of NSC		
Compressive stress, MPa	**Inelastic strain, mm/mm**	**Damage parameter**	**Tensile stress, MPa**	**Crack strain, mm/mm**	**Damage parameter**
37.86	0	0	2.49	0	0
41.31	0.000153	0.053	2.77	0.000006	0.034
43.49	0.000268	0.084	2.97	0.000012	0.057
44.23	0.000428	0.124	3.05	0.000021	0.093
41.25	0.000893	0.228	2.12	0.000098	0.361
35.44	0.001447	0.337	1.45	0.000167	0.534
29.72	0.001999	0.432	0.97	0.000254	0.670
24.97	0.002520	0.509	0.80	0.000307	0.723
21.22	0.003009	0.571	0.74	0.000333	0.743
18.28	0.003472	0.620	0.54	0.000458	0.810
15.96	0.003915	0.660	0.43	0.000580	0.848
14.10	0.004343	0.693	0.36	0.000701	0.873
12.60	0.004760	0.721	0.31	0.000821	0.890
11.36	0.005168	0.744	0.28	0.000941	0.903
7.52	0.007135	0.819	0.25	0.001060	0.913
4.41	0.0109226	0.887	0.23	0.0011795	0.921
3.10	0.0146523	0.918	0.13	0.0023696	0.957
2.38	0.0183630	0.936	0.10	0.0035577	0.970
1.10	0.0368432	0.969	0.06	0.0047452	0.977
0.72	0.0552948	0.980	0.03	0.0059326	0.981

4.2. Plastic parameters of NSC

The CDP model requires five additional parameters, divided into two groups: empirical constants have minimal impact on the finite element simulation and trial parameters play a critical role in simulating the behavior of concrete structures and calculation speed in ABAQUS [39,40]. Empirical constants include flow potential eccentricity (M), the ratio of the second stress invariant on the tensile meridian to that on the compressive meridian such that the maximum principal stress is negative (K_C), the ratio of the initial equiaxial compressive yield stress to the initial uniaxial compressive yield stress (f_{bo} / f_{co}). These parameters were assigned values of 0.1, 0.6667, and 1.16, respectively, for concrete. The viscosity (μ) and dilation angle (ϕ) influence the post-peak behavior of concrete, control the calculation speed, and convergence rate [30]. Based on trial calculations, the viscosity (μ) was set to 0.01 for ease of convergence, while the dilation angle was defined as 40°.

4.3. Constitutive model of steel mesh

For steel meshes, its stress-strain relationship can be set as perfect elastoplastic, as shown in Figure 10. The following Equation (14) was used for the mild steel meshes [41]:

$$f_s = \begin{cases} E_s \varepsilon_s & \text{for } 0 \le \varepsilon_s \le \varepsilon_y \\ f_y & \text{for } \varepsilon_y < \varepsilon \end{cases} \quad (14)$$

where f_s and ε_s = stress and strain in steel, respectively; E_s = modulus of elasticity of steel, set as 210,000 MPa in present study; f_y and ε_y = yield stress and strain, respectively, yield stress was set as 450 MPa in present study.

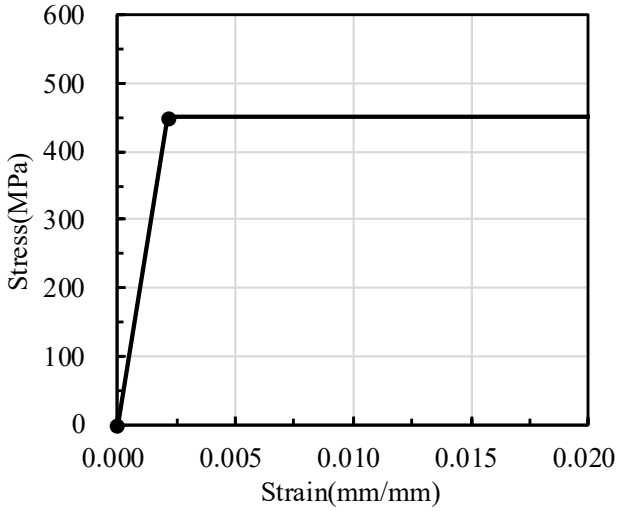

Figure 10. Idealized stress-strain relationships for steel meshes.

5. Validation of numerical analysis and result discussion

The proposed numerical model was validated by comparing its results with experimental results obtained from two 3DPC shear keys [4]. All specimens failed in shear as reported. Table 4 lists two modeling methods with different interface interactions for shear keys with different key angles. Each specimen was given a name including three parts. For example, Numerical-DS-k54-Tie-Co means a finite element modelling shear key with a key angle of 54°, interfaces between 3D-printed and casted concrete were tied together, and interfaces between concrete with epoxy contained both friction and cohesion.

Table 4. Different modelling methods for 3D-printed shear key.

Cases	Interface between 3D-printed and casted concrete	Interface between concrete with epoxy
Numerical-DS-k54-Contact-Co	Contact interaction with friction	Contact interaction with friction and cohesion
Numerical-DS-k54-Tie-Co	Tie	Contact Interaction with friction and cohesion
Numerical-DS-k54-Tie-Fric	Tie	Contact interaction with friction only
Numerical-DS-k70-Contact-Co	Contact interaction with friction	Contact interaction with friction and cohesion
Numerical-DS-k70-Tie-Co	Tie	Contact interaction with friction and cohesion
Numerical-DS-k70-Tie-Fric	Tie	Contact interaction with friction only

5.1. Mesh sensitivity analysis

In this study, five global element sizes, *i.e.*, 5 mm, 7.5 mm, 10 mm, 15 mm, and 20 mm, were selected based on the specimen dimensions for mesh sensitivity analysis.

Figure 11 compares the experimental results of the specimen with a shear key angle of 54° and the numerical simulation results under different element sizes in terms of load-deflection curves. The results

indicate that when the element size is too small (*i.e.*, 5 mm and 7.5 mm), the computation terminates prematurely, failing to reach the target displacement of 6 mm. Although the 7.5 mm mesh achieves good agreement with the experimental data (particularly in the later softening stage), its computational cost is significantly higher than that of the 10 mm mesh, and the 10 mm mesh ensures both convergence and completion of the analysis. For the 15 mm mesh, the computational accuracy is nearly identical to that of the 10 mm mesh, but its predicted peak load is slightly lower than the actual value. The 20 mm mesh effectively captures the ascending branch and peak load but overestimates the residual strength in the softening stage. Therefore, considering both computational efficiency and accuracy, a mesh size of 10 mm was adopted for finite element modeling and further mesh optimization in the present study.

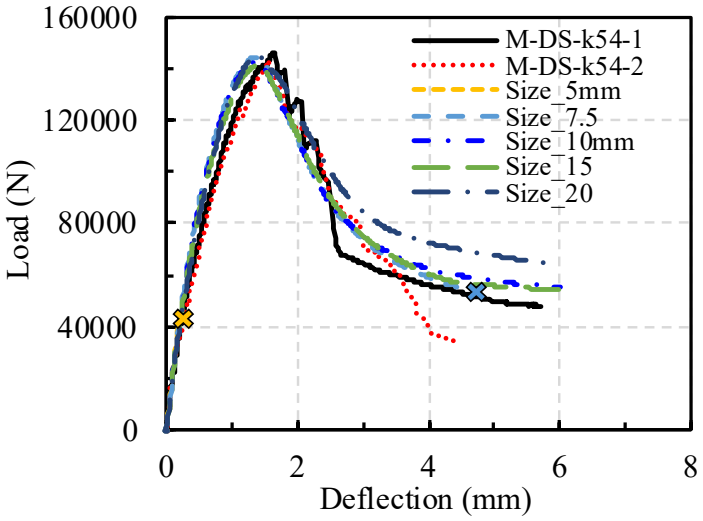

Figure 11. Mesh sensitivity analysis of shear key models.

5.2. Discussion of numerical results

Figure 12 plots the experimental and numerical load-deflection curves for each specimen, with each shear key design having a parallel specimen. As each experimental configuration includes two specimens, the physically tested specimens are labeled using the configuration name followed by the digits “1” and “2”—for example, M-DS-k54-1 and M-DS-k54-2. These labels represent the first and second specimens tested with a shear key angle of 54.46°. Based on the comparison of the test and simulation results in the figure. It can be found that:

(1) Numerical-DS-k54/70-Contact-Co provides the most accurate prediction, capturing both the peak strength and the overall load-deflection curves, including the initial stiffness and the softening segment.

(2) Numerical-DS-k54/70-Tie-Co overestimates the initial stiffness and peak load. This occurs because prohibiting sliding between printed and cast concrete causes the shear key to behave like a rigid body with higher stiffness. Consequently, the predicted curves exhibit a steeper ascending segment and slightly higher peak strength. However, this influence diminishes during the softening segment. This is likely due to the loss of cohesion when the interfaces began to slip. The residual friction of the interfaces was almost the same for all numerical specimens since they used the same friction coefficient.

(3) Numerical-DS-k54-Tie-Fric shows a much lower load-deflection curve than Numerical-DS-k54-Tie-Co due to the absence of cohesion. In contrast, Numerical-DS-k70-Tie-Fric shows a slightly lower curve than Numerical-DS-k70-Tie-Co. Besides, Numerical-DS-k70-Tie-Fric had a similar plastic strain region to Numerical-DS-k70-Tie-Co (*i.e.*, shown in Figure 13c,d). It means that cohesion had little effect on the load-deflection curve before peak. Since higher angles in shear key reduce the bonding effectiveness of epoxy. The reason behind this is that a larger shear key angle reduces interface bonding by distributing shear stress more locally since it has a shorter contact path, which increases stress concentration and local failure. It also decreases the normal force on the interface, reducing frictional resistance.

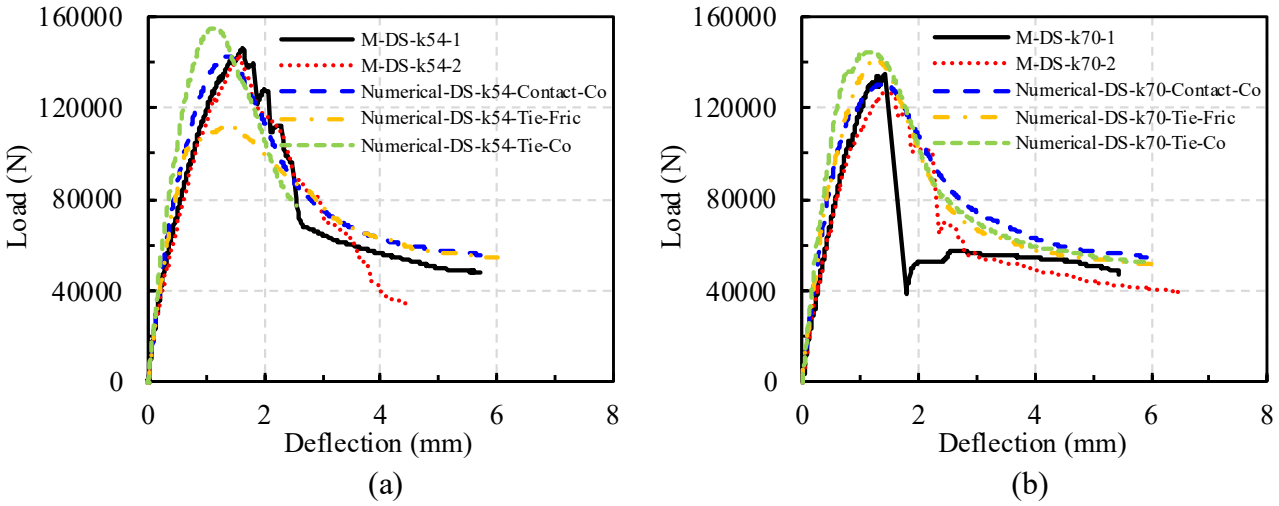

Figure 12. Experimental and numerical load-deflection curves for: **(a)** DS-k54 and **(b)** DS-k70.

Table 5 shows the comparison between the experimental and numerical peak load and deflection for different specimens. It can be found that:

(1) Numerical-DS-k54-Contact-Co shows highest accuracy with the predicted-to-experimental ratio of 0.99 and 0.86 for peak load and deflection, respectively. Numerical-DS-k70-Contact-Co has a ratio of 1.00 and 0.96 for peak load and deflection, respectively.

(2) Ignoring the interaction between printed and cast concrete tends to give a higher peak load between 7% to 10%. Moreover, it tends to give a lower prediction of peak deflection between 21% to 29%. This is because simply tying the concrete surface introduces a higher stiffness of shear key body.

(3) A comparison between Numerical-DS-k54-Tie-Co and Numerical-DS-k54-Tie-Fric reveals that the predicted strength increases by 38.8% due to the presence of interfacial bonding. However, for an inclination angle of 70 degrees, this enhancement decreases to 2.2%. Additionally, the peak displacement also increases. This is attributed to the improved shear resistance and stiffness of the component when interfacial bonding is considered.

(4) For experimental specimens, when the key angles rise from 54° to 70°, the peak load and deflection decrease 10.4% and 10%, respectively.

Table 5. Different modelling methods for 3D-printed shear key.

Cases	Predicted peak load (N)	Exp. (AVE)	Pre. / Exp.	Predicted peak deflection (mm)	Exp. (AVE)	Pre. / Exp.
Numerical-DS-k54-Contact-Co	142747		0.99	1.35992		0.86
Numerical-DS-k54-Tie-Co	155247	144755	1.07	1.1248	1.58775	0.71
Numerical-DS-k54-Tie-Fric	111846		0.77	1.36195		0.86
Numerical-DS-k70-Contact-Co	130693		1.00	1.38788		0.96
Numerical-DS-k70-Tie-Co	144527	131070	1.10	1.1443	1.4445	0.79
Numerical-DS-k70-Tie-Fric	141386		1.08	1.24744		0.86

Note: Exp. = experimental result; Pre. = predicted result; AVE = average value between two tested specimens.

Figure 13 shows the compressive damage, tensile damage, and plastic strain diagrams for each specimen. It can be found that:

(1) Regardless of the modeling method, the results show: (a) the red color region, *i.e.*, highly crushed concrete, for compressive damage diagrams means that concrete crushing is concentrated at the shear key interlock, (b) the red color region, *i.e.*, highly cracked concrete, for tensile damage diagrams means that concrete cracking occurs at the interlock key region and at the top and bottom corners due to bending under eccentric vertical loading, and (c) equivalent plastic strain is concentrated at the interlock, corresponding to shear failure as observed experimentally.

(2) Using the "tie" method to model the interface between the printed and casted concrete results in localized damage at shear key interlock and top/bottom corners. This is because "Tie" method allows uniform strain transfer and makes the strain field more localized. In contrast, allowing sliding at the interface leads to more distributed damage, which aligns better with the experimental results. This phenomenon also can be found in equivalent plastic strain diagrams in Figure 13, where Numerical-DS-k54/70-Contact-Co shows higher plastic strain and larger distribution.

(3) Through equivalent plastic strain diagrams, it can be found that there is a distinct difference for shear keys with a key angle of 54°. When cohesion is included, the plastic strain field is much smaller which shows higher shear capacity for the model with cohesion. However, the equivalent plastic strain diagrams show minimal differences regardless of whether cohesion behavior is included for the shear key with higher key angles as can be seen in Figure 13e,f. This is because cohesion provided by epoxy is less effective for shear key with higher key angles. This phenomenon also can be found in the load-deflection curves shown in Figure 12b in which Numerical-DS-k70-Tie-Fric has a similar peak load to Numerical-DS-k70-Tie-Co.

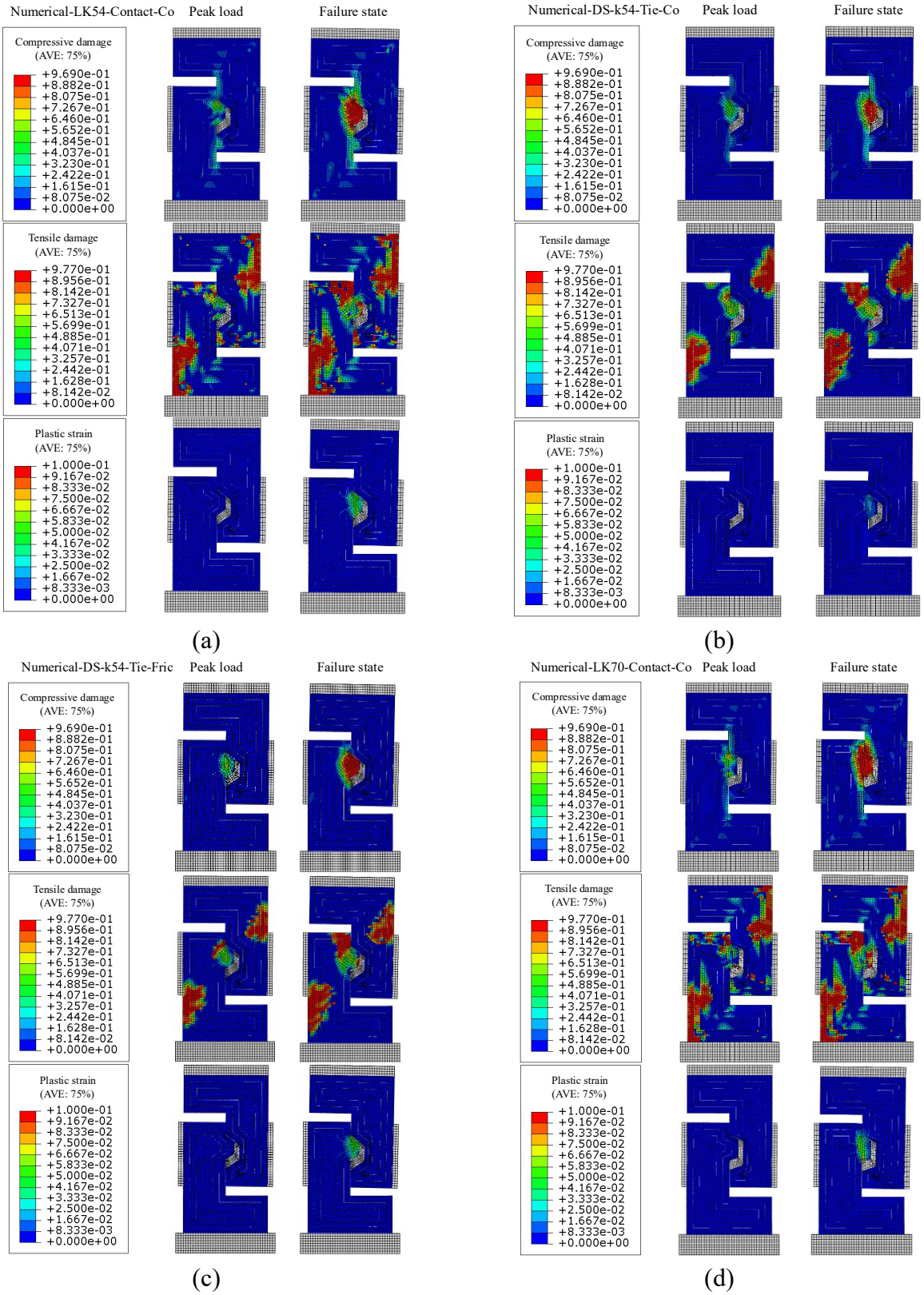

Figure 13. Damage C/T and plastic strain diagrams for DS-k54/70 with different modeling methods at peak and ultimate failure state: **(a)** Numerical-DS-k54-Contact-Co; **(b)** Numerical-DS-k54-Tie-Co; **(c)** Numerical-DS-k54-Tie-Fric; **(d)** Numerical-DS-k70-Contact-Co; **(e)** Numerical-DS-k70-Tie-Co; and **(f)** Numerical-DS-k70-Tie-Fric.

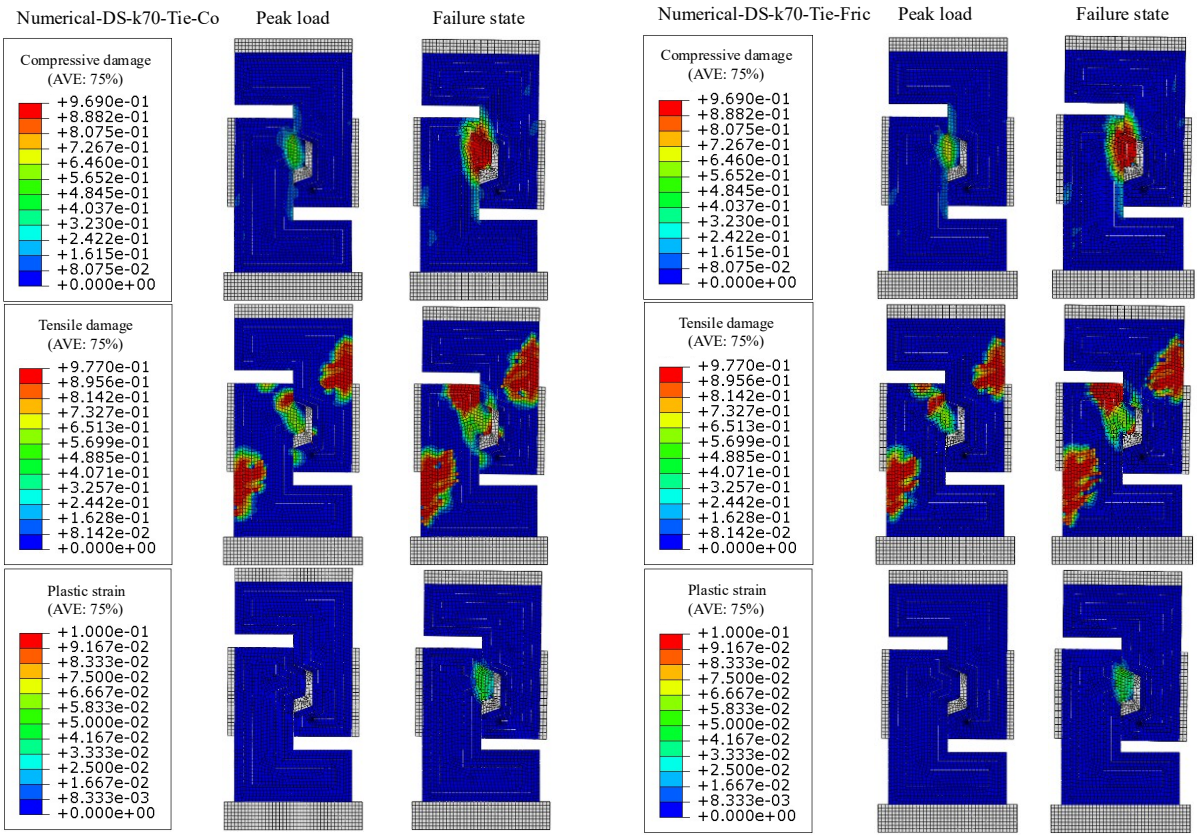

(e) (f)

Figure 13. *Cont.*

Figure 14 further shows the comparison between actual failure behavior and numerical simulations, in which several details were marked. The "Detail A" in Figure 14a means that the crushing of concrete appeared when the specimen was shear off. The "Detail B" in Figure 14b means that the corner of shear key specimens may appear flexural cracks due to the bending moment caused by eccentric loading. The "Detail C" in Figure 14c means that the principal strains were concentrated in the interlock, corresponding to the shear failure.

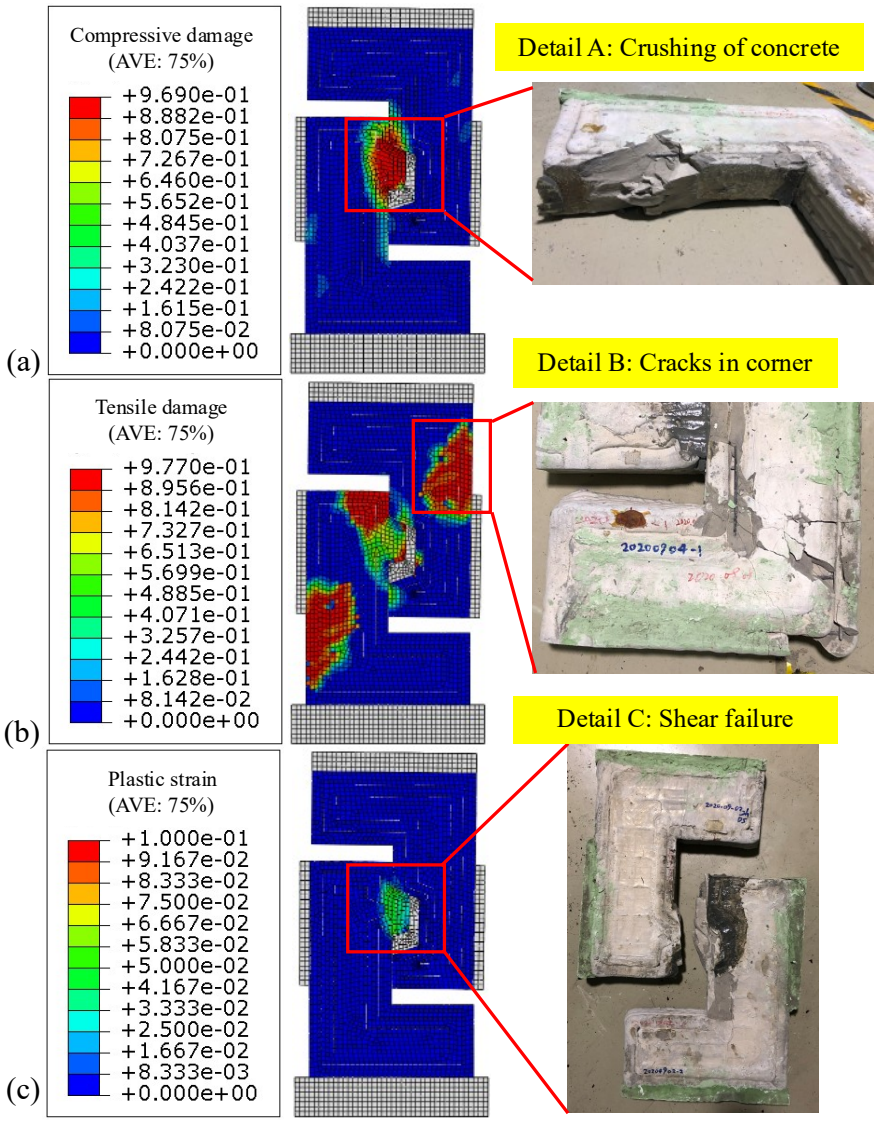

Figure 14. Comparison of experimental and numerical failure patterns for a typical specimen: **(a)** compressive damage; **(b)** tensile damage; and **(c)** equivalent plastic strain.

6. Conclusions

This study briefly introduced the previous work of large-scale concrete shear keys by the corresponding author, *i.e.*, reference [4]. Then, finite element modeling strategies with different interface interactions were established and validated based on previous experimental work. The following conclusions can be drawn from the above experimental and numerical studies:

(1) Both experimental and numerical push-off specimens had similar ascending branches of load-deflection curves followed by different softening segments since the post-peak failure process was relatively brittle. Besides, the failure mode of these specimens was a brittle shear failure triggered by the separation of key regions.

(2) Consider both the cohesion and friction between the interlock interfaces gives more accurate predictions on the shear performance of 3DPC shear key. Besides, Numerical-DS-k54/70-Contact-Co had better performance on prediction since it simulates the interaction behavior between the printed and cast concrete. In contrast, Numerical-DS-k54/70-Tie-Co overestimates the initial stiffness and

peak load. This occurs because prohibiting sliding between printed and casted concrete causes the shear key to behave like a rigid body with higher stiffness. For Numerical-DS-k54-Contact-Co, the predicted-to-experimental ratio of 0.99 and 0.86 for peak load and deflection, respectively.

(3) The modelling strategies did not influence the softening segment prediction since the residual friction of the interfaces was almost the same for these numerical specimens.

(4) Ignoring the interaction between printed and cast concrete tends to give a higher peak load between 7% to 10%. Moreover, it tends to give a lower prediction of peak deflection between 21% to 29%. This is because simply tying the concrete surface introduces a higher stiffness of shear key body.

(5) A higher key angle makes the cohesion provided by epoxy less effective. Since the higher key angle makes the contact paths for interface bonding shorter and the normal force is decreased which has a lower friction which can be seen in both experimental and numerical results. When the key angles rose from 54° to 70°, the peak load and deflection decreased by 10.4% and 10%, respectively.

7. Limitations and future work

This study developed a finite element model for 3D-printed shear keys that accounts for distinct interfacial behaviors. The limitations and future research directions are outlined below:

(1) The validation of the finite element model was limited to experimental data from the 3D-printed shear key study reported in [4]. Although the shear key in that study was designed using established design methods—ensuring it reasonably represents a standard shear key—future work should incorporate additional shear key experiments to more comprehensively verify the model's robustness.

(2) The methodology of determining interfacial friction and cohesive behavior through slant shear tests requires further experimental substantiation.

(3) While this work established and validated finite element modeling framework, subsequent parametric studies are essential to broaden and deepen the investigation of 3D-printed shear keys.

Acknowledgements

This project is supported by the Ministry of Education, Singapore, under the Academic Research Fund Tier 1 (FY2019). The author, Dr. Xin Tian, gratefully acknowledge the support by the China Scholarship Council for studying abroad (project number: 202306130103). The fund sources had no involvement in study design, collection, analysis and interpretation of data; writing of this paper; and in the decision to submit the article for publication.

Authors' contribution

Xin Tian: conceptualization, methodology, investigation, software, data curation, validation, writing—original draft, formal analysis. Anqi Shi: conceptualization, methodology, investigation, data curation, validation, writing-original draft. Zhi Fang: conceptualization, methodology, supervision, writing—review & editing. Alexander Lin: conceptualization, methodology, funding acquisition, resources, supervision, project administration, writing—review & editing.

Conflicts of interests

The authors declare no conflict of interest.

References

[1] Hager I, Golonka A, Putanowicz R. 3D printing of buildings and building components as the future of sustainable construction? *Procedia Eng.* 2016, 151:292–299.

[2] Sepasgozar SME, Shi A, Yang L, Shirowzhan S, Edwards DJ. Additive manufacturing applications for Industry 4.0: a systematic critical review. *Buildings* 2020, 10:231.

[3] Cheng L, Gui Y, Cheng J, Xing M. Experimental and numerical investigation of the shear performance of an innovative keyway joint for prefabricated concrete wall panels. *Buildings* 2023, 13:2978.

[4] Hua T, Lin A, Poh WJD, Wong DHA, Zhang H, *et al*. 3D-printed concrete shear keys: design and experimental study. *Dev. Built Environ.* 2023, 15:100180.

[5] Chen Z, Xiao J, Ding T, Liu B. Push-off test on concrete-concrete interface with different types of concrete after elevated temperatures. *Constr. Build. Mater.* 2023, 377:131157.

[6] Wang L, Liu Y, Yang Y, Li Y, Bai M. Bonding performance of 3D printing concrete with self-locking interfaces exposed to compression–shear and compression–splitting stresses. *Addit. Manuf.* 2021, 42:101992.

[7] Jiang Y, Gao P, Adhikari S, Yao X, Zhou H, *et al*. Studies on the mechanical properties of interlayer interlocking 3D printed concrete based on a novel nozzle. *Case Stud. Constr. Mater.* 2025, 22:e04193.

[8] Mostert JP, Kruger J. Reducing anisotropic behaviour of 3D printed concrete through interlocked filaments. *Mater. Struct.* 2025, 58:192.

[9] Wang Z, Chen Z, Xiao J, Ding T. Experimental study on interfacial shear behavior of 3D printed recycled mortar. *3D Print. Addit. Manuf.* 2024, 11:e1162–e1174.

[10] Licciardello L, Soto AG, Kaufmann W, Metelli G. Determining the strength of 3D printed concrete with the modified slant shear test. *Struct. Concr.* 2025, 26:2467–2486.

[11] Mostafa A, Shankar K, Morozov EV. Influence of shear keys orientation on the shear performance of composite sandwich panel with PVC foam core: numerical study. *Mater. Des.* 2013, 51:1008–1017.

[12] Zhu Y, Zhang Y, Li X, Chen G. Finite element model to predict structural response of predamaged RC beams reinforced by toughness-improved UHPC under unloading status. *Eng. Struct.* 2021, 235:112019.

[13] Zhu Y, Zhang Y, Hussein HH, Chen G. Numerical modeling for damaged reinforced concrete slab strengthened by ultra-high performance concrete (UHPC) layer. *Eng. Struct.* 2020, 209:110031.
[14] Zhang X, Hao H, Zheng J, Hernandez F. The mechanical performance of concrete shear key for prefabricated structures. *Adv. Struct. Eng.* 2021, 24:291–306.
[15] Shamass R, Zhou X, Alfano G. Finite-element analysis of shear-off failure of keyed dry joints in precast concrete segmental bridges. *J. Bridge Eng.* 2015, 20:04014084.
[16] Al-Rousan RZ, Qudaisat MS. Single keyed joints behaviour and capacity formulation under direct shear using non-linear finite-element analysis. *Structures* 2023, 47:911–924.
[17] Zhan Y, Li Z, Chen Z, Shao J, Yue F, *et al*. Experimental and numerical investigations on shear behavior of large keyed tooth joints. *Constr. Build. Mater.* 2022, 344:128200.
[18] Neirinck T, Semendary AA, Murison E, Svecova D. Performance of UHPC shear keys in box girder bridges-field and finite element study. *Eng. Struct.* 2023, 296:116896.
[19] Hussein HH, Walsh KK, Sargand SM, Al Rikabi FT, Steinberg EP. Modeling the shear connection in adjacent box-beam bridges with ultrahigh-performance concrete joints. I: model calibration and validation. *J. Bridge Eng.* 2017, 22:04017043.
[20] Hussein HH, Sargand SM, Al Rikabi FT, Steinberg EP. Experimental validation of optimized ultra-high-performance concrete shear key shape for precast pre-stressed adjacent box girder bridges. *Constr. Build. Mater.* 2018, 190:178–190.
[21] Hussein HH, Sargand SM, Zhu Y, Khoury I, Al Rikabi FT. Experimental and numerical investigation on optimized ultra-high performance concrete shear key with shear reinforcement bar. *Structures* 2022, 40:403–419.
[22] Jiang H, Chen L, Ma ZJ, Feng W. Shear behavior of dry joints with castellated keys in precast concrete segmental bridges. *J. Bridge Eng.* 2015, 20:04014062.
[23] Zhi Q, Xiong X, Yang W, Liu S, Xiong J. Experimental study on the shear behavior of precast wall concrete joints with/without dowel reinforcement. *Materials* 2020, 13:1726.
[24] Ibrahim IS, Padil KH, Bady HMA, Saim AA, Sarbini NN. Ultimate shear capacity and failure of shear key connection in precast concrete construction. *Malays. J. Civil Eng.* 2014, 63.
[25] Feng J, Liang W, Jiang H, Huang C, Zhang J. Shear performance of single-keyed dry joints between reactive power concrete and high strength concrete in push-off tests. *Sci. Prog.* 2020, 103(2):0036850420928643.
[26] Feng J, Hu Z, Jiang H, Hu J, Qiu Y. Influence of RPC grouting materials on shear behavior of wet joints in PCSBs with confining stress. *Constr. Build. Mater.* 2021, 299:123993.
[27] Yuan A, Zhao X, Lu R. Experimental investigation on shear performance of fiber-reinforced high-strength concrete dry joints. *Eng. Struct.* 2020, 223:111159.
[28] Yang IH, Kim KC, Kim YJ. Shear strength of dry joints in precast concrete modules. In *Proceedings of the Thirteenth East Asia-Pacific Conference on Structural Engineering and Construction (EASEC-13)*, Sapporo, Japan, September 11–13, 2013, pp. I-5-3.
[29] Zhou X, Mickleborough N, Li Z. Shear strength of joints in precast concrete segmental bridges. *ACI Struct. J.* 2005, 102(1):3.
[30] Krahl PA, Carrazedo R, El Debs MK. Mechanical damage evolution in UHPFRC: experimental and numerical investigation. *Eng. Struct.* 2018, 170:63–77.

[31] Zhang T, Li X, Hou Z, Chen Q, Fang Y, *et al*. An improved damage plastic model for RC structure FE modelling under cyclic loading conditions. *Eng. Struct.* 2025, 322:119135.

[32] Feghali P, Krahl P, De Andrade Silva F. Optimization of UHPC beams under flexural loading: a numerical and experimental investigation. *Structures* 2024, 68:107115.

[33] De Lima PB, Krahl PA, Silva FA, Cardoso DCT. A modeling strategy for the flexural performance prediction of UHPC beams accounting for variability of properties. *Compos. Struct.* 2023, 322:117374.

[34] Zhang T, Hou Z, Chen Q, Li X, Fang Y, *et al*. A novel damage model integrated into the elastoplastic constitutive model and numerical simulations of reinforced concrete structures under cyclic loading. *J. Build. Eng.* 2024, 84:108670.

[35] AASHTO. *LRFD Bridge Design Specifications*, 8th ed. Washington: American Association of State Highway and Transportation Officials, 2017. p. 1781.

[36] ACI Committee 318. *Building Code Requirements for Structural Concrete (ACI 318–19) and Commentary*. Farmington Hills (MI): American Concrete Institute, 2019.

[37] Zhu Y, Zhang Y, Shi J. Finite element analysis of flexural behavior of precast segmental UHPC beams with prestressed bolted hybrid joints. *Eng. Struct.* 2021, 238:111492.

[38] Ministry of Housing and Urban-Rural Development, Beijing, China. Code for design of concrete structures (GB/T50010-2010), 2023.

[39] Jabbar AM, Hamood MJ, Mohammed DH. Impact of dilation angle and viscosity on the ultra-high performance concrete behavior in Abaqus. In *2021 International Conference on Advance of Sustainable Engineering and Its Application (ICASEA)*, Wasit, Iraq, October 27–28, 2021, pp. 125–130.

[40] Mahdi AM. Impact of failure-surface parameters of concrete damage plasticity model on the behavior of reinforced ultra-high performance concrete beams. *Period. Polytech. Civil Eng.* 2023, 67(2):495–504.

[41] Holzer S, Baker R, Somers A. *SINDER: A computer code for general analysis of two-dimensional reinforced concrete structures*. New Mexico: Air Force Weapens Laboratory, 1975.